ACS ES&T Air

Open Access

pubs.acs.org/estair

Article

# Quantifying $NO_x$ Emission Sources in Houston, Texas Using Remote Sensing Aircraft Measurements and Source Apportionment Regression Models

Daniel L. Goldberg,* Benjamin de Foy, M. Omar Nawaz, Jeremiah Johnson, Greg Yarwood, and Laura Judd

Cite This: *ACS EST Air* 2024, 1, 1391−1401

Read Online

ACCESS | Metrics & More | Article Recommendations | Supporting Information

**ABSTRACT:** Air quality managers in areas exceeding air pollution standards are motivated to understand where there are further opportunities to reduce $NO_x$ emissions to improve ozone and $PM_{2.5}$ air quality. In this project, we use a combination of aircraft remote sensing (i.e., GCAS), source apportionment models (i.e., CAMx), and regression models to investigate $NO_x$ emissions from individual source-sectors in Houston, TX. In prior work, GCAS column $NO_2$ was shown to be close to the "truth" for validating column $NO_2$ in model simulations. Column $NO_2$ from CAMx was substantially low biased compared to Pandora (−20%) and GCAS measurements (−31%), suggesting an underestimate of local $NO_x$ emissions. We applied a flux divergence method to the GCAS and CAMx data to distinguish the linear shape of major highways and identify $NO_2$ underestimates at highway locations. Using a multiple linear regression (MLR) model, we isolated on-road, railyard, and "other" $NO_x$ emissions as the likeliest cause of this low bias, and simultaneously identified a potential overestimate of shipping $NO_x$ emissions. Based on the MLR, we modified on-road and shipping $NO_x$ emissions in a new CAMx simulation and increased the background $NO_2$, and better agreement was found with GCAS measurements: bias improved from −31% to −10% and $r^2$ improved from 0.78 to 0.80. This study outlines how remote sensing data, including fine spatial information from newer geostationary instruments, can be used in concert with chemical transport models to provide actionable information for air quality managers to identify further opportunities to reduce $NO_x$ emissions.

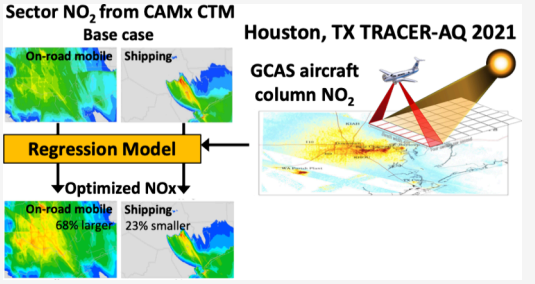


**KEYWORDS:** *Urban air pollution, $NO_x$ emissions, Nitrogen dioxide, Column $NO_2$, GCAS, CAMx model, Flux divergence*

## INTRODUCTION

Exposure to $NO_x$ ($NO_x$ = NO + $NO_2$) is associated with asthma exacerbation in vulnerable groups[1,2] and premature death.[3,4] $NO_x$ emissions are also a critical participant in ozone formation, another toxic air pollutant.[5−7] Many North American cities already have $NO_x$-limited ozone formation during the warm season,[8−10] and the remaining cities should have primarily $NO_x$-limited conditions in the coming years.[11] Further reducing ozone pollution in metropolitan areas will therefore require improved quantification of $NO_x$ emissions. One major limitation of our current observing network is the inability to accurately quantify $NO_x$ emissions on a sector-by-sector basis in a timely fashion, with the exception of continuous emissions monitoring systems (CEMS) on electricity generating units. Additionally, many nonroad sources of $NO_x$ emissions, such as industrial or construction emissions, have large uncertainties.[12]

Typically, air pollutant emission rates for chemical species such as $NO_x$ are estimated using a "bottom-up" approach, which uses fuel consumption information, spatial surrogates (e.g., road density, population density, locations of known stack emissions), temporal surrogates (e.g., traffic patterns, industrial work schedules) and emission factors (mass of pollutant per mass of fuel burned) to estimate the spatiotemporal patterns of emissions across regions.[13,14] With investments in technology to better understand the spatiotemporal patterns of pollutants (e.g., incorporating real-time traffic data using speed and type of vehicle) and laboratory studies to better estimate the emission factors in a wide range of conditions, these "bottom-up" estimates can be improved.[15] These new and improved estimates can then be incorporated into a chemical transport model and evaluated against observations from ground monitors. Based on this comparison, the emission estimates can be further adjusted and improved if necessary. However, given the complexity of this cycle,

Received: May 1, 2024
Revised: September 27, 2024
Accepted: September 30, 2024
Published: October 15, 2024

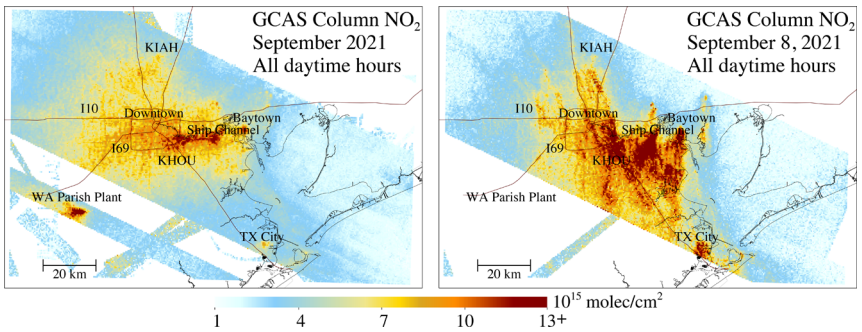


**Figure 1.** GCAS column $NO_2$ measurements during the September 2021 Houston TRACER-AQ field campaign. The left panel shows all GCAS measurements during ten flight days between September 1−26, 2021 averaged together. The right panel shows all measurements during the September 8, 2021 flight day averaged together. Areas of large $NO_x$ emissions are labeled on both panels. Maps are created using IDL (https://www.nv5geospatialsoftware.com/Products/IDL).

"bottom-up" emission estimates typically take many years to compile by a large team of scientists, and subsequently, are delayed in time by several years from the actual emission time.

A complementary method to estimate air pollutant emissions is in using a "top-down" approach. With this method, emissions are back calculated from pollutant measurements acquired across an entire airshed. This is typically done with a remote sensing instrument−in orbit[16−18] or on an aircraft.[19−21] Analyses have been conducted for global megacities[22−26] and power plants[27,28] using the Tropospheric Monitoring Instrument (TROPOMI) and a complementary satellite instrument, the Ozone Monitoring Instrument (OMI). The emission rates are inferred by analyzing the concentration maps over a large region and incorporating the lifetime (chemical and dispersion lifetime) of the pollutant to back-calculate the emission rate at the source. The advantage of a "top-down" technique is that it is independent of the complex data sets needed to estimate "bottom-up" emissions rates. Typically these aggregated "top-down" estimates agree with the "bottom-up" estimates within 40% in North American cities (well within the uncertainty associated with the "top-down" method).[16,29] Given TROPOMI's spatial resolution (3.5 × 5.5 $km^2$ at nadir) and temporal resolution (once daily), TROPOMI is most often used to calculate total emissions aggregated over the entire metropolitan area and seasonal/annual time scales, and assumptions are needed to infer emissions rate during morning and evening hours. Therefore, very limited, if any, sectoral or hourly information can be gleaned from an analysis using polar-orbiting satellite data sets, such as TROPOMI.

In this project we used fine spatial resolution nitrogen dioxide ($NO_2$) information (250 × 560 $m^2$) from the Geostationary Coastal and air pollution events Airborne Simulator (GCAS) instrument,[30,31] available during the September 2021 Tracking Aerosol Convection ExpeRiment − Air Quality (TRACER-AQ) field campaign,[32] to better understand the fine-scale structure of $NO_x$ emissions in the Houston metropolitan area including a sector-by-sector analysis. Complementing the airborne observations, we perform a simulation using the Comprehensive Air Quality Model with Extensions (CAMx) at fine spatial resolution (444 × 444 $m^2$). The model output has already been compared to data from GCAS and TROPOMI in a complementary paper.[33] In this project, we push further by using source-tagged $NO_2$ information from CAMx and GCAS data to estimate more accurate contributions from different $NO_x$ emission sectors. We do this by using flux divergence methods on the GCAS data and by training a multiple linear regression model to the airborne retrievals, with the CAMx source-tagged $NO_2$ as the independent variables.

## METHODS

**GCAS.** The GCAS instrument was installed on the NASA G-V aircraft during the TRACER-AQ field campaign in Houston, Texas during September 2021. The GCAS instrument employs charge-coupled device array detectors to observe backscattered light. These data can be used to calculate column densities of gases, such as $NO_2$, below the aircraft using differential optical absorption spectroscopy (DOAS).[34]

During TRACER-AQ, GCAS collected data over the Houston metropolitan area across 12 days during late August and throughout September 2021. The flight strategy of the aircraft included flying the plane in a "lawnmower" fashion with flight lines spaced 6.3 km apart, ensuring overlap at flight altitude (28,000 feet) with the instrument field of view of 45 deg creating one gapless map of $NO_2$ up to three times per flight day. GCAS has a native pixel resolution of approximately 250 m × 560 m at flight altitude. Observations from two of the flight days—a test flight (August 30) and a flight over the Gulf of Mexico (September 27) are excluded from this study because they provided sparse data over Houston. Given the relatively short time frame of flight data collection; meteorological conditions have an influence on the fine-scale patterns in $NO_2$ columns observations.

Air mass factors (AMFs) use modeled scattering weights and vertical profile information to account for altitude-dependent sensitivities in remote-sensing observations.[35,36] The original vertical profiles in the data set were derived from a global model, GEOS-CF,[37] that had a coarser spatial resolution (0.25° × 0.25°), but in this study we only show GCAS column $NO_2$ measurements processed with vertical profile information from CAMx. To directly compare GCAS measurements to the CAMx $NO_2$ column concentrations we regrid them to the fine-scale WRF-CAMx grid. Only cloud-free GCAS data is considered in this analysis. An example of daily and monthly averaged GCAS data is shown in Figure 1. The differences in these two time scales highlights the complexity of $NO_2$ variance in cities, such as Houston. September 8, 2021 was chosen because it was a day with clear skies, and winds were northerly allowing for the point source $NO_2$ plumes along the Ship Channel to have less mixing with the downtown $NO_2$


https://doi.org/10.1021/acsestair.4c00097
ACS EST Air 2024, 1, 1391−1401

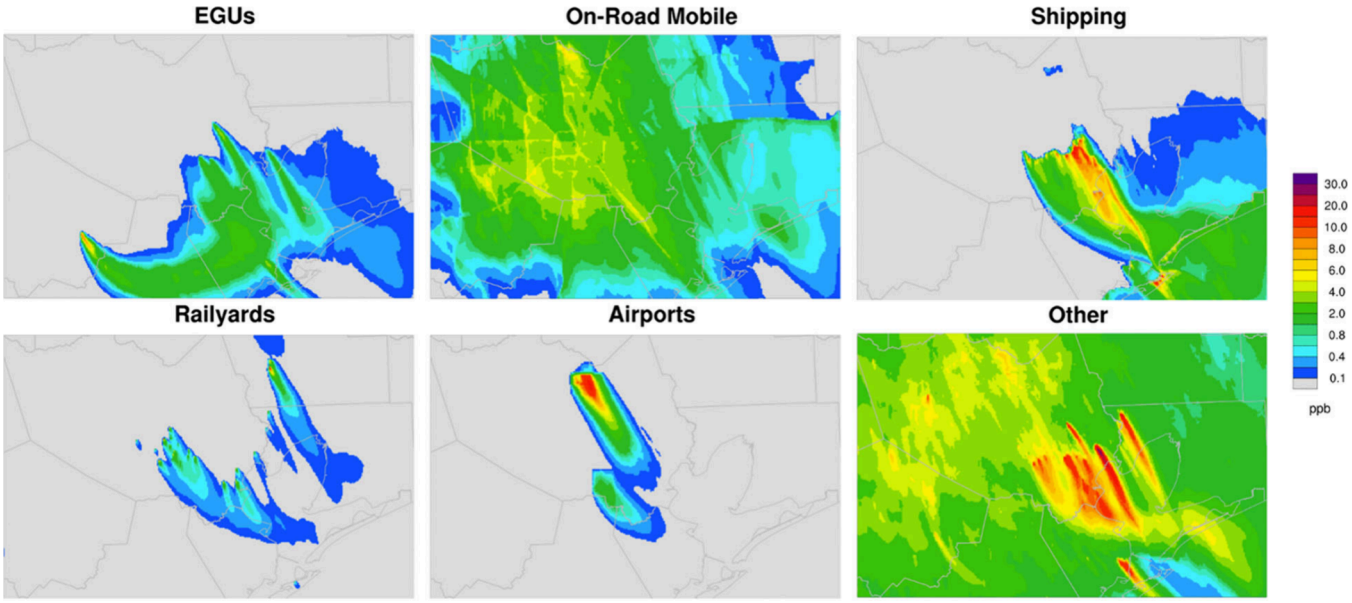


**Figure 2.** Examples of six of the CAMx tagged surface $NO_2$ concentrations at 8:00 AM local time on September 8, 2021 in Houston (spatial domains are the same as Figure 1). Maps are created using NCL (http://dx.doi.org/10.5065/D6WD3XH5).

plume. A description of the landmark acronyms can be found in Table S1. Diurnal column $NO_2$ patterns are shown in Figure S1.

**Pandora.** Pandora instruments are ground-based upward-looking spectrometers measuring spectrally resolved radiances that are converted into slant column $NO_2$ amounts using differential optical absorption spectroscopy in a similar manner as a remote sensing instrument, such as TROPOMI.[38] Observations from three Pandora monitoring sites were available during the TRACER-AQ field campaign to validate the GCAS, satellite, and model column $NO_2$ measurements. Critical to this project, we found in previous work[33] that the GCAS measurements of column $NO_2$ during the TRACER-AQ campaign had an excellent correlation ($r^2$ = 0.79) and minimal normalized mean bias (NMB = +3.4%) when compared to measurements of the same quantity from Pandora instruments, suggesting that the GCAS measurements acquired during the TRACER-AQ campaign are very close to the "truth". The Pandora instruments were located in the suburban and urban neighborhoods.

**WRF-CAMx Simulation.** For this study, a set of simulations were conducted employing version 4.3.3 of the Advanced Research Weather Research and Forecasting (WRF) model[39] jointly with the Comprehensive Air Quality Model with Extensions (CAMx) v7.20[40] with the CB6r5 chemical mechanism for a simulation period that matched the September 2021 TRACER-AQ domain and time frame. The 36/12/4/1.33/0.444 km model domains can be seen in Nawaz et al.[33] Prior work evaluated this WRF simulation and found minimal systematic biases in surface-level wind speed, direction, temperature, and water vapor mixing ratio compared to observations from 16 ground-level monitors.[33] A longer description of the WRF-CAMx model options can be found in the Supporting Information. For emissions in CAMx, we start with an emissions inventory developed by the TCEQ for the Dallas-Fort Worth (DFW) and Houston-Galveston-Brazoria (HGB) Attainment Demonstration (AD) SIP revisions and implement further minor changes as discussed in the Supplemental.

**Source Apportionment.** We used the CAMx ozone source apportionment tool (OSAT)[41] to track $NO_2$ from several emission source sectors. OSAT is a tagged-species method for online source apportionment that operates in parallel with the core model simulation.[42] The tagged nitrogen species used for this analysis is named RGN in OSAT and includes $NO_2$, gas phase $NO_3$, and $N_2O_5$ with the latter two components being in negligible concentrations during the daytime periods of our analysis. We therefore refer to tagged RGN and $NO_2$ interchangeably. The tagged NOx emission source sectors are listed in Table S2. To select individual electric generating units (EGUs) in our 0.444 km CAMx domain for $NO_2$ tracking we used a threshold of 0.8 tons per day of $NO_x$ emissions. This threshold identified nine EGUs shown in the first nine rows of Table S2. We also selected on-road mobile, railyards, shipping and the George Bush Intercontinental (KIAH) and William P. Hobby (KHOU) airports for $NO_2$ tracking. All remaining $NO_x$ emissions were tracked together in the "other" category. Relevant for this project, average weekday $NO_x$ emissions for the 0.444 m domain were 302 tons per day (123 Gg/yr). The total amount of $NO_x$ emissions in each sector can be seen in Table S3 and Figures S2 and S3. Examples of the $NO_2$ source apportionment can be seen in Figure 2.

**Flux Divergence Top-down Emissions Calculation.** The flux divergence method can identify point sources in the TROPOMI $NO_2$ retrievals with higher resolution than averaged vertical column densities. The method was first applied over Riyadh, Germany and South Africa to estimate $NO_x$ emissions from large point sources.[18,28] Due to TROPOMI's higher spatial resolution compared with OMI, the flux divergence method can identify emissions within individual urban areas.[29,43−45]

The flux divergence method works best with long temporal averages; for TROPOMI analyses, annual or multiyear averages are used. We adapted the method[43] for the current project to handle GCAS data from 27 individual scenes spanning 10 days. We found that the method worked best when the GCAS data was oversampled to the 444 × 444 $m^2$



https://doi.org/10.1021/acsestair.4c00097
ACS EST Air 2024, 1, 1391−1401

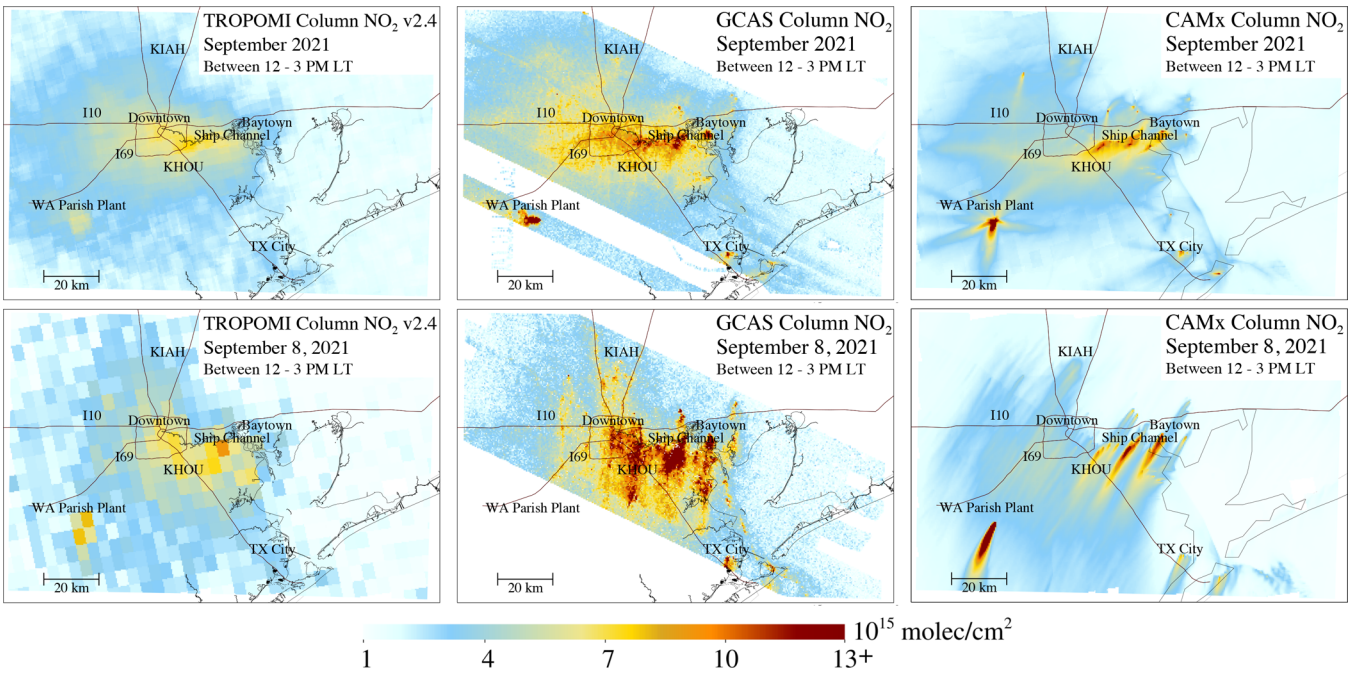


**Figure 3.** Column $NO_2$ over Houston from two remote sensing observational platforms, and CAMx model simulation in the early afternoon: 12−3 PM local time. The left column shows measurements from TROPOMI, the center column shows measurements from GCAS, and the right column shows the CAMx model. The top row shows measurements during all 10 flight days in September 2021, while the bottom row shows September 8, 2021 only. Maps are created using IDL (https://www.nv5geospatialsoftware.com/Products/IDL).

CAMx grid. Only pixels with an aircraft roll angle below 0.5° were used. We interpolated the WRF-CAMx winds to the time of the GCAS overpass. After extensive testing with different options, we found that using the WRF winds from the seventh model layer gave the clearest results but that the method was robust with respect to the specific layer used. Although prior work with TROPOMI obtained clearer results by performing the flux divergence in swath coordinates (along and across track),[42] we found that doing this increased the noise in the results for the GCAS retrievals. We therefore used second-order differences performed along the x/y axes (i.e., using the cells to the north, south, east, and west of the central cell) as well as along the cross directions (i.e., using the cells to the northeast, southeast, southwest and northwest of the central cell). The fluxes were calculated by multiplying the vertical $NO_2$ column with the WRF wind speed at the selected height (layer 7 ≈ 370 m) and then scaling with a NOx to $NO_2$ ratio of 1.32. Averaging both the x/y estimate and the cross-estimate led to smoother divergence fields with less noise. The flux divergence fields were used to show patterns of emissions but not to make quantitative estimates of emissions. We therefore display the flux divergence terms without the lifetime parameter, following Beirle et al.[28]

The method was initially performed using the GCAS standard retrievals and the ERA5 wind reanalysis product.[46] We found that the level of noise was reduced, and the known sources were better identified when we used the GCAS retrievals that were corrected using the CAMx AMFs, and when we used the WRF-CAMx meteorology, since it represented the daily transport patterns and boundary layer height more accurately. These sensitivity tests revealed that CAMx simulations can be used to yield clear improvements in the flux divergence method.

**Multiple Linear Regression Model.** For this study, we built a multiple linear regression (MLR) model to find the optimal combination of the sectoral emissions simulated by CAMx that matches the GCAS tropospheric vertical columns. A MLR was chosen because it is a simple way to quantify individual linear scaling factors for each CAMx sector without including the complexity of nonlinear factors and interaction parameters between variables. The model assumes that emission adjustments are time-invariant. CAMx simulations were made in Source Apportionment mode to separate the $NO_2$ vertical column densities associated with the 15 individual sources (e.g., EGU) and groups of sources (on-road mobile) (Table S5). In practice, some of the emission sources in OSAT are too close together to be able to be clearly distinguished from each other. We therefore merged the following: 1. Channelview Cogeneration Facility and Odyssey Energy Altura Cogen, LLC; 2. Deer Park Energy Center and Pasadena Power Plant; 3. Texas City Cogeneration, South Houston Green Power Site, and the "other" category. Equation 1 shows the MLR model: the tropospheric vertical column density of GCAS is represented as an optimal combination of the CAMx vertical column densities from the 10 contributing sectors with a residual given by $\varepsilon$. In seeking an optimal match to the GCAS columns, it is important to apply a regularization term to prevent unphysical results.[47] The optimal parameters ($\beta$) were determined by minimizing the cost function in eq 2. The residual $\varepsilon$ is minimized subject to the regularization term $\lambda$ applied to the magnitude of the scale factors ($\beta$). Equation 2 can be solved in a single Least Squares inversion.[47] We applied the MLR model to the entire field campaign, and we also performed simulations separately for weekdays and for weekends.

$$\mathrm{VCD}_{\mathrm{GCAS}} = \sum_{i=1}^{10} \beta_i \mathrm{VCD}_{\mathrm{CAMx},i} + \varepsilon \quad (1)$$



https://doi.org/10.1021/acsestair.4c00097
ACS EST Air 2024, 1, 1391−1401

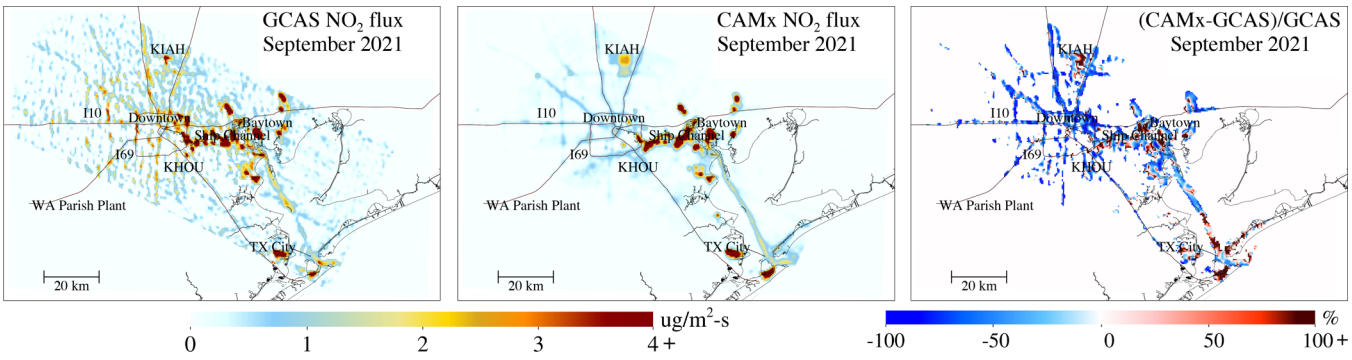


**Figure 4.** The left panel shows the net $NO_2$ fluxes ($\mu g/m^2$-s) using the FD method applied to all GCAS measurements. Fluxes are positive when there are $NO_x$ emissions originating from a grid cell. Negative fluxes represent a net $NO_x$ sink in a grid cell but are screened out for clarity. The center panel shows the net $NO_2$ fluxes ($\mu g/m^2$) using the FD method applied to all coincident CAMx output. The right panel is the ratio (CAMx-GCAS)/GCAS in areas where the GCAS $NO_2$ fluxes are >0.2 $\mu g/m^2$-s. Maps are created using IDL (https://www.nv5geospatialsoftware.com/Products/IDL).

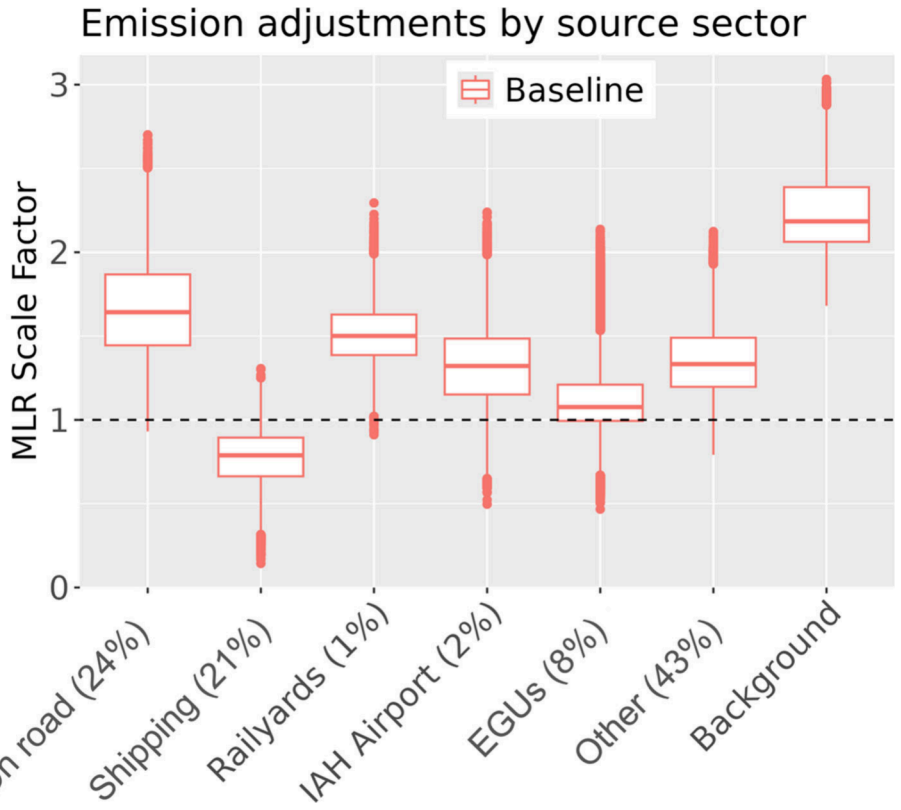


**Figure 5.** Box-and-whisker plot of scaling factors obtained from the multilinear regression model with 100 bootstrapped selection of rasters each consisting of 100 bootstrapped selection of grid blocks included in the analysis. Percentages show the fraction of domain-wide NOx emissions from each sector.

$$J = \|\varepsilon\|_2 + \lambda^2 \|\beta\|_2 \quad (2)$$

The regularization term, $\lambda$ in eq 2, imposes a cost on the departure of the posterior emissions from the prior emissions. In this work, we chose a value of 25 because it balances the desire to maximize the improvements in the model (lower grid residuals) while minimizing the departure from the prior (lower emission residuals). By selecting this value, we achieve most of the improvements in the correlation coefficient of the model without ending up with unrealistic scaling factors. The algorithm then balances the cost in the change of the emissions with the cost of the mismatch between the GCAS retrievals and the sum of the scaled fields from the source apportionment simulations. We assume as a prior that all scaling factors are 1.

## RESULTS AND DISCUSSION

The first step in this project is to qualitatively compare the GCAS column $NO_2$ measurements with coincident measurements from TROPOMI and model output from CAMx. The TROPOMI $NO_2$ tropospheric vertical column measurement was recalculated using AMFs derived from vertical profile information from CAMx. Spatial plots of column $NO_2$ in the early afternoon at the TROPOMI overpass time are shown in Figure 3 for a 10-day average and a single day. By observing the 10-day average (top row), we can see that GCAS


https://doi.org/10.1021/acsestair.4c00097
ACS EST Air 2024, 1, 1391−1401

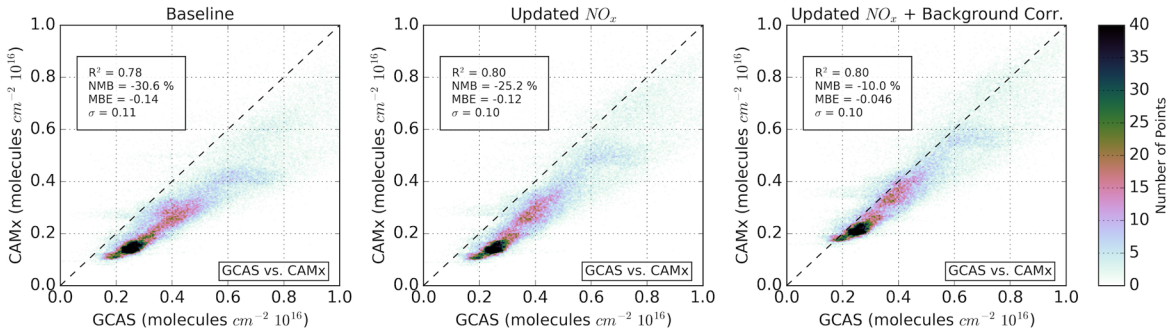


**Figure 6.** CAMx column $NO_2$ evaluated against the same quantity from GCAS measurements. The left panel is the baseline simulation and recreated from Nawaz et al. (2024). The center panel is the "optimized $NO_x$" simulation (1.68x on-road mobile and 0.77x shipping). The right panel is "optimized $NO_x$" simulation + an additional 0.7 × $10^{15}$ background column $NO_2$ using the scaling factor from the MLR.

measurements are generally larger than both the TROPOMI measurements and CAMx model output. TROPOMI captures the broad spatial patterns observed by GCAS with a notable low bias. The TROPOMI low bias is partially driven by the 3.5 × 5.5 $km^2$ spatial resolution at nadir (marginally larger along the swath edges) which is unable to capture the peaks of the $NO_2$ pollution, especially the $NO_2$ in narrow point source plumes.[48] Previous work shows that the AMFs are a small contributor—less than 10%—to this low satellite bias in this area,[33] but this can vary by region.[49] An underestimate of TROPOMI $NO_2$ measurements in polluted areas is consistent with comparisons completed by the TROPOMI Cal-Val team.[50]

The GCAS versus CAMx intercomparison suggests that the point source plumes are captured well by the model, but that $NO_2$ is severely underestimated in the downtown area of Houston, as well as in the outer portions of the model domain. This suggests two issues with the $NO_2$ in CAMx: an underestimate of $NO_x$ emissions near downtown Houston, and an underestimate of $NO_2$ advected into the model domain from the boundary conditions. In following sections, we explore these model biases quantitatively.

**$NO_x$ Emissions Using Flux Divergence Applied to GCAS.** The flux divergence (FD) method applied to the GCAS aircraft data revealed patterns of $NO_2$ fluxes ($\mu g/m^2$) in the greater Houston area. To our knowledge, this paper is the first to calculate $NO_2$ fluxes by applying the FD method to aircraft remote sensing data. As noted above, although the FD method applied to such a short time period suffers from noise in the data, there are nevertheless clear patterns that emerge. We restricted the colorbar to positive values as this made the plots clearer. We identified many of the major $NO_x$ sources individually in the Houston CAMx domain: power plants and refineries as well as the IAH international airport (Figure 4, left panel). In addition, the method identified the area of the ship channel as well as the route of the ships sailing through the Galveston Bay. Finally, the method clearly identified the major highways in the region. The center panel of Figure 4 shows the flux divergence method applied to the CAMx simulation. In this case, the sources are known and so these simulations serve to evaluate the accuracy of the method. The method clearly recovers the main point and line sources used in the CAMx simulations. The right panel of Figure 4 shows the ratio of the $NO_2$ flux divergence (i.e., (CAMx-GCAS)/GCAS) for the GCAS grid cells exceeding 0.2 $\mu g\text{-}m^2\text{-}s^{-1}$. Over the large point sources near the ship channel, the values are a mix of positive and negative values suggesting that the emissions inventory is relatively accurate in this location. Over highways, the values are strongly negative suggesting that actual on-road emissions may be underestimated in the current inventory used as input to the CAMx model. In theory, the 444 m spatial resolution model should be capturing the near-road $NO_2$ concentrations with the same precision as the GCAS which has similar spatial resolution. Over the ship paths, especially closer to the Gulf of Mexico, the values are positive suggesting that some of the ship $NO_x$ emissions may be overestimated in the inventory. These conclusions are only representative of the 10 days of September 2021 and not any other time frame.

**Use of Machine Learning to Estimate Emission Factors for Individual Sectors.** We applied the MLR model to CAMx source apportionment $NO_2$ sectoral output and GCAS $NO_2$ data, as shown in eqs 1 and 2, to estimate scaling factors for the sectoral $NO_2$. All median scaling factors were between a value of 0.5 and 2.5 as shown in Figure 5. A median value below 1 indicates the sector needs a $NO_x$ decrease, while a median value greater than 1 indicates the sector needs a $NO_x$ increase. The box-and-whisker plots represent the uncertainties of the scaling factors quantified by bootstrapping on two different levels. The most important level for bootstrapping was randomly selecting, with replacement, the GCAS rasters included in the optimization. For the full time series, there were 27 rasters over 10 days. In addition to performing the simulations for these 27 rasters, we performed 100 simulations with random selections of the 27 rasters. The second level for bootstrapping was to randomly select grid blocks within each raster for use in the analysis. We randomly select 7 × 7 blocks of cells within the CAMx grid cells and include them until we have the same number of points as in the initial grid. We did this 100 times for each selection of rasters, leading to a total of 10,000 simulations. The bootstrapping procedure accounts for the uncertainty due to scene selection as well as due to geographic location within a scene. It therefore includes a measure of the uncertainty due to variations in meteorology and variations in emissions from one scene to the next, and a measure of the uncertainty due to source intensities and chemical regimes within each scene. It does not include the impact of the regularization parameter ($\lambda$).

The box-and-whisker plots in Figure 5 show that on-road mobile $NO_x$ emissions representing 24% of domain emissions may be underestimated in the model and need to be scaled up by a median factor of 1.68, which is consistent with findings using the FD method. Similarly, the MLR found railyard $NO_x$


https://doi.org/10.1021/acsestair.4c00097
ACS EST Air 2024, 1, 1391−1401

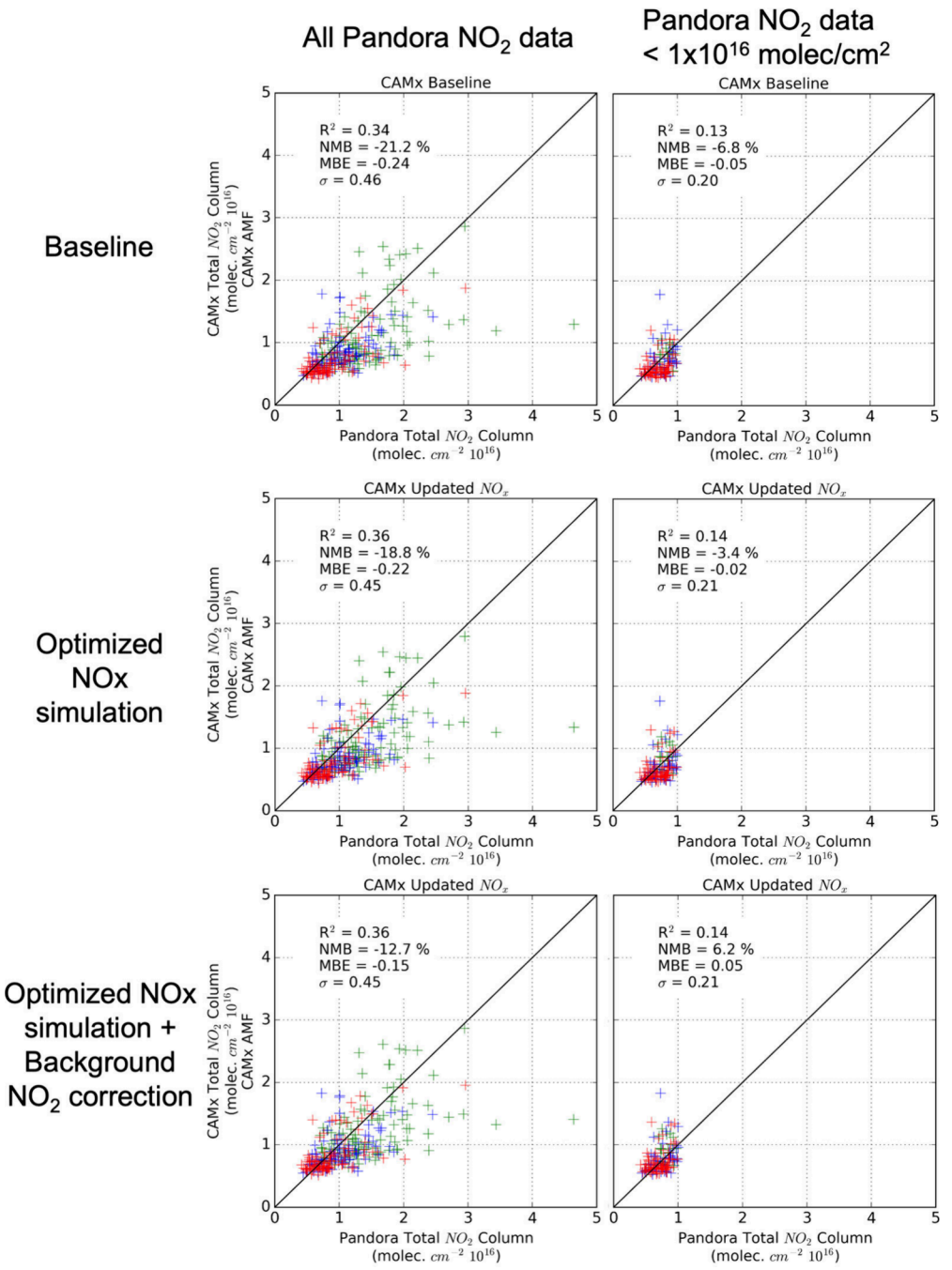


**Figure 7.** CAMx vs Pandora total column $NO_2$ intercomparisons. The left column shows intercomparisons during all conditions. The right column shows intercomparisons during moderately polluted and clean conditions ($<10 \times 10^{15}$ molec/cm$^2$). The top row shows the baseline CAMx simulation and recreated from Nawaz et al. (2024). The middle row shows the "optimized NOx" CAMx simulation. The bottom row shows the "optimized NOx" CAMx simulation + background $NO_2$ correction (a uniform addition of $0.7 \times 10^{15}$ molec/cm$^2$). Different colors represent the three Pandora measurement sites as discussed in Nawaz et al. (2024).

emissions should by increased by a median factor of 1.5. In contrast, the shipping $NO_x$ emissions representing 21% of domain emissions may be overestimated and should be scaled by a median factor of 0.77, which is also consistent with findings using the FD method, though it should be noted that the sign of the shipping scaling factor changes with the regularization term. The EGU point sources are close to a scale factor of 1, which is expected given the use of emissions obtained from Continuous Emissions Monitoring System measurements. The "other" sources representing 43% of domain $NO_x$ emissions are underestimated, although this factor is particularly sensitive to the regularization term because it encompasses a diverse set of point and nonpoint sources. Finally, the boxplot suggests that the $NO_2$ background concentration is underestimated by CAMx by a median value of $0.7 \times 10^{15}$ molec/cm$^2$, which equates to a scaling factor of 2.2, and is consistent with qualitative findings discussed earlier.

**Results from an "Optimized $NO_x$" CAMx Simulation.** We then performed a new "optimized NOx" CAMx simulation with on-road mobile and shipping $NO_x$ emissions adjusted to be in alignment with findings from using the MLR. On-road mobile $NO_x$ emissions for both weekdays and weekends were


https://doi.org/10.1021/acsestair.4c00097
ACS EST Air 2024, 1, 1391−1401

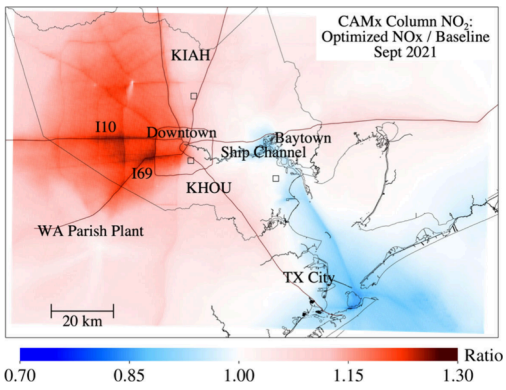


**Figure 8.** Column $NO_2$ ratio plot between the CAMx "optimized NOx" simulation vs CAMx baseline simulation during the early afternoon (12:00–15:00 local time). The map was created using IDL (https://www.nv5geospatialsoftware.com/Products/IDL).

increased by a factor of 1.68, and shipping $NO_x$ emissions were decreased by multiplying by a factor of 0.77. Despite a large change to the on-road $NO_x$, the total $NO_x$ emissions in the domain only increased by 11% from 302 to 334 tons per day (Table S3). We chose not to adjust the railyards and airport sectors because combined they represent less than 3% of domain NOx emissions. We chose not to adjust the "other" sector or background/boundary $NO_2$ since there is no straightforward modification for those contributions. In previous work,[33] we found better agreement between GCAS and CAMx on the weekend, but since there were only 3 weekend days (2 Saturdays and 1 Sunday) used in this analysis, we could not disentangle the meteorological influences that may have caused better agreement on these days. Therefore, we are not able to conclusively state that NOx emission modifications should be different on weekends than weekdays.

When comparing the column $NO_2$ from the baseline and "optimized NOx" simulations to the GCAS measurements, we found better agreement and an improvement in bias, albeit a smaller improvement than we had expected (Figure 6). The column $NO_2$ low bias improved from −31% to −25% with a small increase in correlation from $r^2 = 0.78$ to $r^2 = 0.80$. When we further add an artificial $0.7 \times 10^{15}$ molec/cm$^2$ column $NO_2$ enhancement domain-wide—value acquired from the MLR—the $NO_2$ low bias improves further to −10%. The remaining low bias is likely due to not adjusting the "other" $NO_x$ emissions, which represented 43% of domain $NO_x$ emissions in the baseline simulation.

When comparing the column $NO_2$ from the baseline and "optimized NOx" simulations to the Pandora measurements, we found better agreement and an improvement in bias, albeit a smaller improvement than we had expected (Figure 7). The column $NO_2$ low bias improved from −20% to −18% with a small increase in correlation from $r^2 = 0.39$ to $r^2 = 0.41$. However, much of the apparent low bias appears to be driven by the large Pandora measured values. We then exclude values exceeding $10 \times 10^{15}$ molec/cm$^2$—which approximate fine-scale $NO_2$ plumes that we cannot expect CAMx to recreate in space due to the need to match wind speed and direction.[51] For moderately polluted scenes (values $<10 \times 10^{15}$), the $NO_2$ low bias is only −7%. When evaluating the new model simulation improved from −7% to −3%; the correlation is notably poor in both scenarios due to the smaller range of values.

Figure 8 shows a ratio difference plot of modeled column $NO_2$ between the baseline and "optimized NOx" simulations.

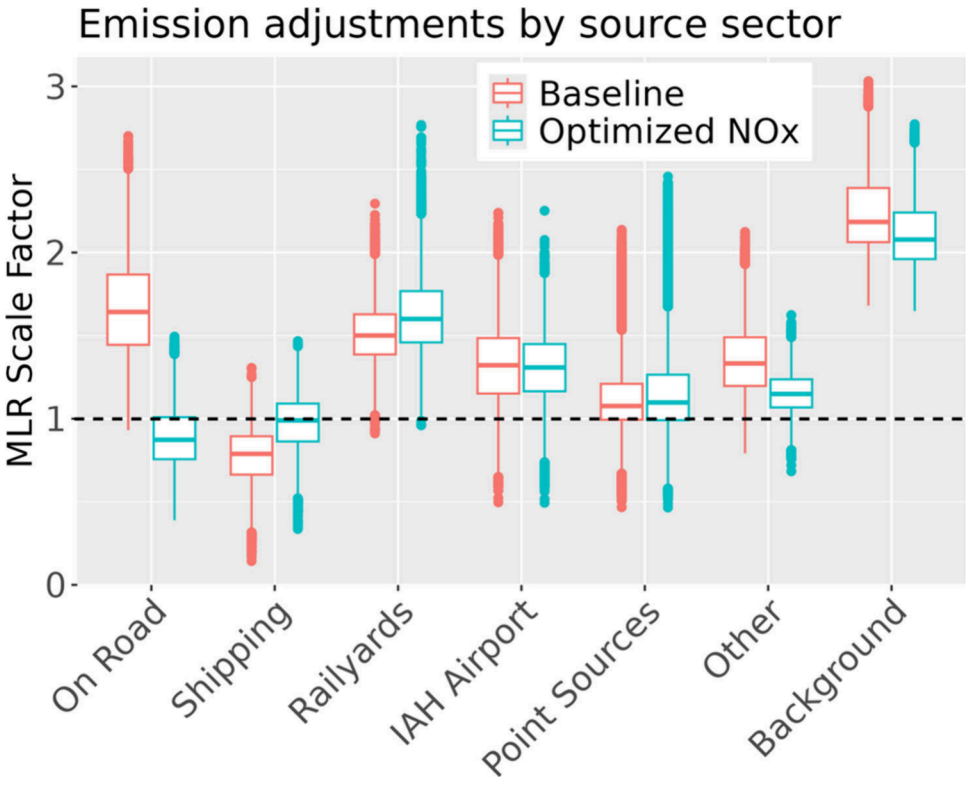


**Figure 9.** Box-and-whisker plot of scaling factors of the baseline and updated CAMx simulation obtained from the multilinear regression model with 100 bootstrapped selection of rasters and 100 bootstrapped selection of grid blocks to include in the analysis.


https://doi.org/10.1021/acsestair.4c00097
ACS EST Air 2024, 1, 1391−1401

The largest $NO_2$ enhancements in the "optimized $NO_x$" simulation occurred in areas of west Houston where there were no Pandora measurements (denoted as square boxes on the figure). The maximum change in column $NO_2$ was an increase of 30% in west Houston near a major highway intersection, with a median column $NO_2$ enhancement of +4% across the full model domain. Although the model domain $NO_x$ emissions increased +11%, column $NO_2$ only increased +4% because a substantial amount of $NO_2$ originates beyond the model domain.

When comparing the MLR results between the baseline and optimized NOx simulations, we see substantial improvement in the coefficients attributed to on-road and shipping emissions (Figure 9), while all other coefficients remain largely steady. This indicates both the robustness of the method as well as a strong indication that the adjustments made to the $NO_x$ emissions were appropriate. The on-road $NO_x$ emissions may have been slightly overcorrected, and the "other" $NO_x$ emissions still need an adjustment up. As expected, the coefficient attributed to the background $NO_2$ did not change, and this would be more difficult to control without modifying the boundary conditions or the $NO_2$ lifetime. A longer discussion on the influence of $NO_2$ long-range transport on the MLR can be found in the Supporting Information.

**Discussion.** In this project, we were able to conduct a thorough analysis of $NO_x$ emissions in Houston, Texas during September 2021 during the TRACER-AQ campaign. Prior work found column $NO_2$ from GCAS to have excellent agreement with Pandora measurements ($r^2 = 0.79$ and NMB of +2.4%),[33] suggesting it can be used as the "truth" in validating the column $NO_2$ CAMx model simulation. Column $NO_2$ from CAMx showed a substantial low bias when compared with Pandora (−20%) and GCAS measurements (−31%), suggesting an underestimate of local $NO_x$ emissions.

This study expands upon previous work[33] by applying additional measures to identify and quantify the magnitude of $NO_x$ emissions. The FD method was able to distinguish the linear shape of major highways, many of the large point sources, and the Galveston Bay ship track. The $NO_2$ FD comparison between CAMx and GCAS shows underestimates at highway locations. Through a multiple linear regression model, we were able to isolate on-road, railyard, and "other" $NO_x$ emissions as the likeliest cause of this low bias, while simultaneously finding that shipping $NO_x$ emissions may be overestimated. A new "optimized $NO_x$" simulation was performed with on-road $NO_x$ emissions increased by a factor of 1.68 and shipping $NO_x$ emissions decreased by a factor of 0.77, and confirmed that these $NO_x$ adjustments made to the inventory were reasonable and yielded better agreement with $NO_2$ measurements acquired during the TRACER-AQ campaign.

To our knowledge, this is the first time a source apportionment model was coupled with aircraft measurements to identify uncertainties in the gridded $NO_x$ emissions inventory. Our analyses were primarily conducted using column $NO_2$ instead of surface $NO_2$ to diagnose $NO_x$ emissions since vertical mixing can be a source of error in a surface-only comparison. With finer spatial resolution and more numerous $NO_2$ measurements now available from Tropospheric Emissions: Monitoring of Pollution (TEMPO) starting in August 2023, it is feasible that a similar analysis could be conducted using satellite data. This project provides an fine-scale independent evaluation of the "bottom up" emissions inventories relied upon by policymakers who are looking to understand where there are further opportunities to reduce $NO_x$ emissions and improve ozone and $PM_{2.5}$ air quality in metropolitan areas.

## ■ ASSOCIATED CONTENT

### Data Availability Statement

$NO_2$ observations from GCAS are available here: 10.5067/ASDC/SUBORBITAL/TRACERAQ/DATA001/GV/AircraftRemoteSensing/GCAS_1. The publicly available GCAS measurements (version R2) include a version of the data set with reprocessed AMFs to include $NO_2$ vertical profile estimates from the fine-scale (444 × 444 $m^2$) WRF-CAMx simulation used in this analysis. TROPOMI $NO_2$ column data are publicly available from the Copernicus Data Space Ecosystem: https://dataspace.copernicus.eu. Pandora $NO_2$ data are available here: https://asdc.larc.nasa.gov/project/TRACER-AQ/TRACERAQ_Pandora_Data_1. WRF-CAMx output for $NO_2$ and $O_3$ are available upon request.

### Supporting Information

The Supporting Information is available free of charge at https://pubs.acs.org/doi/10.1021/acsestair.4c00097.

A description of landmark acronyms, a spatial map of the diurnal pattern of column $NO_2$ as observed by GCAS, a description of the WRF-CAMx model setup, satellite-derived $NO_X$ emissions for the Houston, TX area, spatial images of the sector column $NO_2$ before and after MLR adjustment, and a sensitivity study of the influence of $NO_2$ long-range transport on the MLR (PDF)

## ■ AUTHOR INFORMATION


### Corresponding Author

**Daniel L. Goldberg** − *Department of Environmental and Occupational Health, George Washington University, Washington, D.C. 20052, United States;* orcid.org/0000-0003-0784-3986; Email: dgoldberg@gwu.edu

### Authors

**Benjamin de Foy** − *Department of Earth and Atmospheric Sciences, Saint Louis University, St. Louis, Missouri 63103, United States;* orcid.org/0000-0003-4150-9922

**M. Omar Nawaz** − *Department of Environmental and Occupational Health, George Washington University, Washington, D.C. 20052, United States;* orcid.org/0000-0001-7706-7287

**Jeremiah Johnson** − *Ramboll Americas Engineering Solutions, Novato, California 94945, United States*

**Greg Yarwood** − *Ramboll Americas Engineering Solutions, Novato, California 94945, United States;* orcid.org/0000-0002-4201-3649

**Laura Judd** − *NASA Langley Research Center, Hampton, Virginia 23681, United States*

Complete contact information is available at: https://pubs.acs.org/10.1021/acsestair.4c00097


### Author Contributions

D.L.G., L.J., B.d.F., and G.Y. developed the project design. J.J. and G.Y. set up and conducted the WRF-CAMx simulations. L.J. and the TRACER-AQ science team measured and processed the GCAS and Pandora Data. D.L.G downloaded and processed the TROPOMI $NO_2$ data and regridded all data to the WRF-CAMx grid. B.d.F. performed the flux divergence



https://doi.org/10.1021/acsestair.4c00097
ACS EST Air 2024, 1, 1391−1401

and ran the regression model. D.L.G., B.d.F., and M.O.N. developed figures for the manuscript. D.L.G. and B.d.F. wrote the paper. All authors edited the manuscript.

### Notes

The authors declare no competing financial interest.

## ■ ACKNOWLEDGMENTS

The authors of this paper would like to acknowledge the NASA Tropospheric Composition Program and the Texas Commission on Environmental Quality for TRACER-AQ support and the TRACER-AQ science team for their useful contributions. The preparation of this manuscript was funded by a grant from the Texas Air Quality Research Program (AQRP) at The University of Texas at Austin through the Texas Emission Reduction Program (TERP) and the Texas Commission on Environmental Quality (TCEQ). The findings, opinions and conclusions are the work of the authors and do not necessarily represent findings, opinions, or conclusions of the AQRP or the TCEQ. The authors also acknowledge funding from the NASA Atmospheric Composition Modelling and Analysis Program (ACMAP) (80NSSC23K1002) and the NASA Health and Air Quality Applied Sciences Team (HAQAST) (80NSSC21K0511). This work contains modified Copernicus Sentinel-5 Precursor data processed by KNMI and postprocessed by George Washington University.

## ■ REFERENCES

(1) Achakulwisut, P.; Brauer, M.; Hystad, P.; Anenberg, S. C. Global, National, and Urban Burdens of Paediatric Asthma Incidence Attributable to Ambient $NO_2$ Pollution: Estimates from Global Datasets. *Lancet Planet Health* **2019**, *3*, e166.

(2) Anenberg, S. C.; Mohegh, A.; Goldberg, D. L.; Kerr, G. H.; Brauer, M.; Burkart, K.; Hystad, P.; Larkin, A.; Wozniak, S.; Lamsal, L. Long-Term Trends in Urban NO2 Concentrations and Associated Paediatric Asthma Incidence: Estimates from Global Datasets. *Lancet Planet Health* **2022**, *6* (1), e49−e58.

(3) Huang, K.; Zhu, Q.; Lu, X.; Gu, D.; Liu, Y. Satellite-Based Long-Term Spatiotemporal Trends in Ambient NO2 Concentrations and Attributable Health Burdens in China From 2005 to 2020. *Geohealth* **2023**, *7* (5), No. e2023GH000798.

(4) Camilleri, S. F.; Kerr, G. H.; Anenberg, S. C.; Horton, D. E. All-Cause NO2-Attributable Mortality Burden and Associated Racial and Ethnic Disparities in the United States. *Environ. Sci. Technol. Lett.* **2023**, *10*, 1159.

(5) Turner, M. C.; Jerrett, M.; Pope, C. A.; Krewski, D.; Gapstur, S. M.; Diver, W. R.; Beckerman, B. S.; Marshall, J. D.; Su, J.; Crouse, D. L.; Burnett, R. T. Long-Term Ozone Exposure and Mortality in a Large Prospective Study. *Am. J. Respir Crit Care Med.* **2016**, *193* (10), 1134−1142.

(6) Malley, C. S.; Henze, D. K.; Kuylenstierna, J. C. I.; Vallack, H. W.; Davila, Y.; Anenberg, S. C.; Turner, M. C.; Ashmore, M. R. Updated Global Estimates of Respiratory Mortality in Adults ≥ 30Years of Age Attributable to Long-Term Ozone Exposure. *Environ. Health Perspect* **2017**, *125* (8), No. 087021.

(7) Lim, C. C.; Hayes, R. B.; Ahn, J.; Shao, Y.; Silverman, D. T.; Jones, R. R.; Garcia, C.; Bell, M. L.; Thurston, G. D. Long-Term Exposure to Ozone and Cause-Specific Mortality Risk in the U.S. *Am. J. Respir Crit Care Med.* **2019**, *200*, 1022.

(8) Jin, X.; Fiore, A.; Boersma, K. F.; Smedt, I. De; Valin, L. Inferring Changes in Summertime Surface Ozone−NO x − VOC Chemistry over U.S. Urban Areas from Two Decades of Satellite and Ground-Based Observations. *Environ. Sci. Technol.* **2020**, *54* (11), 6518−6529.

(9) Simon, H.; Reff, A.; Wells, B.; Xing, J.; Frank, N. Ozone Trends across the United States over a Period of Decreasing NOx and VOC Emissions. *Environ. Sci. Technol.* **2015**, *49* (1), 186−195.

(10) Simon, H.; Hogrefe, C.; Whitehill, A.; Foley, K. M.; Liljegren, J.; Possiel, N.; Wells, B.; Henderson, B. H.; Valin, L. C.; Tonnesen, G.; Appel, K. W.; Koplitz, S. Revisiting Day-of-Week Ozone Patterns in an Era of Evolving US Air Quality. *Atmos Chem. Phys.* **2024**, *24* (3), 1855−1871.

(11) Koplitz, S.; Simon, H.; Henderson, B.; Liljegren, J.; Tonnesen, G.; Whitehill, A.; Wells, B. Changes in Ozone Chemical Sensitivity in the United States from 2007 to 2016. *ACS Environmental Au* **2022**, *2*, 206−222.

(12) Zawacki, M.; Baker, K. R.; Phillips, S.; Davidson, K.; Wolfe, P. Mobile Source Contributions to Ambient Ozone and Particulate Matter in 2025. *Atmos. Environ.* **2018**, *188*, 129−141.

(13) McDuffie, E. E.; Smith, S. J.; O'Rourke, P.; Tibrewal, K.; Venkataraman, C.; Marais, E. A.; Zheng, B.; Crippa, M.; Brauer, M.; Martin, R. V. A Global Anthropogenic Emission Inventory of Atmospheric Pollutants from Sector- and Fuel-Specific Sources (1970−2017): An Application of the Community Emissions Data System (CEDS). *Earth Syst. Sci. Data* **2020**, *12* (4), 3413−3442.

(14) Crippa, M.; Guizzardi, D.; Muntean, M.; Schaaf, E.; Dentener, F.; van Aardenne, J. A.; Monni, S.; Doering, U.; Olivier, J. G. J.; Pagliari, V.; Janssens-Maenhout, G. Gridded Emissions of Air Pollutants for the Period 1970–2012 within EDGAR v4.3.2. *Earth Syst. Sci. Data* **2018**, *10* (4), 1987−2013.

(15) Crippa, M.; Guizzardi, D.; Pisoni, E.; Solazzo, E.; Guion, A.; Muntean, M.; Florczyk, A.; Schiavina, M.; Melchiorri, M.; Hutfilter, A. F. Global Anthropogenic Emissions in Urban Areas: Patterns, Trends, and Challenges. *Environmental Research Letters* **2021**, *16* (7), No. 074033.

(16) Goldberg, D. L.; Lu, Z.; Streets, D. G.; de Foy, B.; Griffin, D.; McLinden, C. A.; Lamsal, L. N.; Krotkov, N. A.; Eskes, H. Enhanced Capabilities of TROPOMI $NO_2$: Estimating $NO_X$ from North American Cities and Power Plants. *Environ. Sci. Technol.* **2019**, *53* (21), 12594−12601.

(17) Beirle, S.; Boersma, K. F.; Platt, U.; Lawrence, M. G.; Wagner, T. Megacity Emissions and Lifetimes of Nitrogen Oxides Probed from Space. *Science (1979)* **2011**, *333* (6050), 1737−1739.

(18) Beirle, S.; Borger, C.; Dörner, S.; Li, A.; Hu, Z.; Liu, F.; Wang, Y.; Wagner, T. Pinpointing Nitrogen Oxide Emissions from Space. *Sci. Adv.* **2019**, *5* (11), No. eaax9800.

(19) Kuhlmann, G.; Chan, K. L.; Donner, S.; Zhu, Y.; Schwaerzel, M.; Dörner, S.; Chen, J.; Hueni, A.; Nguyen, D. H.; Damm, A.; Schütt, A.; Dietrich, F.; Brunner, D.; Liu, C.; Buchmann, B.; Wagner, T.; Wenig, M. Mapping the Spatial Distribution of NO2 with in Situ and Remote Sensing Instruments during the Munich NO2 Imaging Campaign. *Atmos Meas Tech* **2022**, *15* (6), 1609−1629.

(20) Meier, A. C.; Schönhardt, A.; Bösch, T.; Richter, A.; Seyler, A.; Ruhtz, T.; Constantin, D.-E.; Shaiganfar, R.; Wagner, T.; Merlaud, A.; Van Roozendael, M.; Belegante, L.; Nicolae, D.; Georgescu, L.; Burrows, J. P. High-Resolution Airborne Imaging DOAS Measurements of NO2 above Bucharest during AROMAT. *Atmos Meas Tech* **2017**, *10* (5), 1831−1857.

(21) Souri, A. H.; Choi, Y.; Pan, S.; Curci, G.; Nowlan, C. R.; Janz, S. J.; Kowalewski, M. G.; Liu, J.; Herman, J. R.; Weinheimer, A. J. First Top-Down Estimates of Anthropogenic NOx Emissions Using High-Resolution Airborne Remote Sensing Observations. *Journal of Geophysical Research: Atmospheres* **2018**, *123* (6), 3269−3284.

(22) Goldberg, D. L.; Lu, Z.; Oda, T.; Lamsal, L. N.; Liu, F.; Griffin, D.; McLinden, C. A.; Krotkov, N. A.; Duncan, B. N.; Streets, D. G. Exploiting OMI NO2 Satellite Observations to Infer Fossil-Fuel CO2 Emissions from U.S. Megacities. *Science of The Total Environment* **2019**, *695*, No. 133805.

(23) Lu, Z.; Streets, D. G.; de Foy, B.; Lamsal, L. N.; Duncan, B. N.; Xing, J. Emissions of Nitrogen Oxides from US Urban Areas: Estimation from Ozone Monitoring Instrument Retrievals for 2005−2014. *Atmos Chem. Phys.* **2015**, *15* (18), 10367−10383.

(24) Liu, F.; Beirle, S.; Joiner, J.; Choi, S.; Tao, Z.; Knowland, K. E.; Smith, S. J.; Tong, D. Q.; Ma, S.; Fasnacht, Z. T.; Wagner, T. High-Resolution Mapping of Nitrogen Oxide Emissions in Large US Cities



https://doi.org/10.1021/acsestair.4c00097
*ACS EST Air* 2024, 1, 1391−1401

from TROPOMI Retrievals of Tropospheric Nitrogen Dioxide Columns. *Atmos Chem. Phys.* **2024**, *24* (6), 3717−3728.
(25) Goldberg, D. L.; Anenberg, S. C.; Lu, Z.; Streets, D. G.; Lamsal, L. N.; E McDuffie, E.; Smith, S. J. Urban NOx Emissions around the World Declined Faster than Anticipated between 2005 and 2019. *Environmental Research Letters* **2021**, *16* (11), No. 115004.
(26) Goldberg, D. L.; Saide, P. E.; Lamsal, L. N.; de Foy, B.; Lu, Z.; Woo, J.-H.; Kim, Y.; Kim, J.; Gao, M.; Carmichael, G. R.; Streets, D. G. A Top-down Assessment Using OMI NO2 Suggests an Underestimate in the NOx Emissions Inventory in Seoul, South Korea, during KORUS-AQ. *Atmos Chem. Phys.* **2019**, *19* (3), 1801−1818.
(27) de Foy, B.; Lu, Z.; Streets, D. G.; Lamsal, L. N.; Duncan, B. N. Estimates of Power Plant NOx Emissions and Lifetimes from OMI NO2 Satellite Retrievals. *Atmos. Environ.* **2015**, *116* (2), 1−11.
(28) Beirle, S.; Borger, C.; Jost, A.; Wagner, T. Improved Catalog of NOx Point Source Emissions (Version 2). *Earth Syst. Sci. Data* **2023**, *15* (7), 3051−3073.
(29) Goldberg, D. L.; Harkey, M.; de Foy, B.; Judd, L.; Johnson, J.; Yarwood, G.; Holloway, T. Evaluating NOx Emissions and Their Effect on O3 Production in Texas Using TROPOMI NO2 and HCHO. *Atmos Chem. Phys.* **2022**, *22* (16), 10875−10900.
(30) Janz, S.; Kowalewski, M. G.; Lamsal, L. N.; Nowlan, C.; Judd, L. M. Airborne Hyperspectral Trace Gas Sensors as Testbeds for Geostationary Air Quality Missions. In *Sensors, Systems, and Next-Generation Satellites XXIII*; Neeck, S. P., Kimura, T., Martimort, P., Eds.; SPIE: 2019; Vol. *11151*, p 86. DOI: 10.1117/12.2533765.
(31) Nowlan, C. R.; Liu, X.; Janz, S. J.; Kowalewski, M. G.; Chance, K. V.; Follette-Cook, M. B.; Fried, A.; González Abad, G.; Herman, J. R.; Judd, L. M.; Kwon, H.-A. A.; Loughner, C. P.; Pickering, K. E.; Richter, D.; Spinei, E.; Walega, J.; Weibring, P.; Weinheimer, A. J. Nitrogen Dioxide and Formaldehyde Measurements from the GEOstationary Coastal and Air Pollution Events (GEO-CAPE) Airborne Simulator over Houston, Texas. *Atmos Meas Tech* **2018**, *11* (11), 5941−5964.
(32) Judd, L.; Sullivan, J. *TRACER-AQ − TRacking Aerosol Convection ExpeRiment − Air Quality*. https://www-air.larc.nasa.gov/missions/tracer-aq/ (accessed August 9, 2022).
(33) Nawaz, M. O.; Johnson, J.; Yarwood, G.; de Foy, B.; Judd, L.; Goldberg, D. L. An Intercomparison of Satellite, Airborne, and Ground-Level Observations with WRF−CAMx Simulations of NO2 Columns over Houston, Texas, during the September 2021 TRACER-AQ Campaign. *Atmos Chem. Phys.* **2024**, *24* (11), 6719−6741.
(34) Platt, U.; Stutz, J. Differential Optical Absorption Spectroscopy. *Differential Optical Absorption Spectroscopy* **2008**, DOI: 10.1007/978-3-540-75776-4.
(35) Judd, L. M.; Al-Saadi, J. A.; Janz, S. J.; Kowalewski, M. G.; Pierce, R. B.; Szykman, J. J.; Valin, L. C.; Swap, R.; Cede, A.; Mueller, M.; Tiefengraber, M.; Abuhassan, N.; Williams, D. Evaluating the Impact of Spatial Resolution on Tropospheric NO2 Column Comparisons within Urban Areas Using High-Resolution Airborne Data. *Atmos. Meas. Tech* **2019**, *12*, 6091−6111.
(36) Judd, L. M.; Al-Saadi, J. A.; Szykman, J. J.; Valin, L. C.; Janz, S. J.; Kowalewski, M. G.; Eskes, H. J.; Veefkind, J. P.; Cede, A.; Mueller, M.; Gebetsberger, M.; Swap, R.; Pierce, R. B.; Nowlan, C. R.; Abad, G. G.; Nehrir, A.; Williams, D. Evaluating Sentinel-5P TROPOMI Tropospheric NO2 Column Densities with Airborne and Pandora Spectrometers near New York City and Long Island Sound. *Atmos Meas Tech* **2020**, *13* (11), 6113−6140.
(37) Keller, C. A.; Knowland, K. E.; Duncan, B. N.; Liu, J.; Anderson, D. C.; Das, S.; Lucchesi, R. A.; Lundgren, E. W.; Nicely, J. M.; Nielsen, E.; Ott, L. E.; Saunders, E.; Strode, S. A.; Wales, P. A.; Jacob, D. J.; Pawson, S. Description of the NASA GEOS Composition Forecast Modeling System GEOS-CF v1.0. *J. Adv. Model Earth Syst* **2021**, *13*, No. e2020MS002413.
(38) Herman, J. R.; Cede, A.; Spinei, E.; Mount, G.; Tzortziou, M. A.; Abuhassan, N. K. NO $_2$ Column Amounts from Ground-Based Pandora and MFDOAS Spectrometers Using the Direct-Sun DOAS Technique: Intercomparisons and Application to OMI Validation. *J. Geophys Res.* **2009**, *114* (D13), No. D13307.
(39) Skamarock, W. C.; Klemp, J. B.; Dudhia, J.; Gill, D. O.; Liu, Z.; Berner, J.; Wang, W.; Powers, J. G.; Duda, M. G.; Barker, D. M.; Huang, X.-Y. *A Description of the Advanced Research WRF Model Version 4*; 2021. http://library.ucar.edu/research/publish-technote.
(40) Ramboll. CAMx User's Guide Version 6.50. http://www.camx.com/files/camxusersguide_v6-50.pdf.
(41) Ramboll. CAMx User's Guide Version 7.20. 2022, No. April.
(42) Dunker, A. M.; Yarwood, G.; Ortmann, J. P.; Wilson, G. M. Comparison of Source Apportionment and Source Sensitivity of Ozone in a Three-Dimensional Air Quality Model. *Environ. Sci. Technol.* **2002**, *36* (13), 2953−2964.
(43) de Foy, B.; Schauer, J. J. An Improved Understanding of NOx Emissions in South Asian Megacities Using TROPOMI NO2 Retrievals. *Environmental Research Letters* **2022**, *17* (2), No. 024006.
(44) Lonsdale, C. R.; Sun, K. Nitrogen Oxides Emissions from Selected Cities in North America, Europe, and East Asia Observed by the TROPOspheric Monitoring Instrument (TROPOMI) before and after the COVID-19 Pandemic. *Atmos Chem. Phys.* **2023**, *23* (15), 8727−8748.
(45) Sun, K. Derivation of Emissions from Satellite-Observed Column Amounts and Its Application to TROPOMI NO2 and CO Observations. *Geophys. Res. Lett.* **2022**, *49*, No. e2022GL101102.
(46) Hersbach, H.; Bell, B.; Berrisford, P.; Hirahara, S.; Horányi, A.; Muñoz-Sabater, J.; Nicolas, J.; Peubey, C.; Radu, R.; Schepers, D.; Simmons, A.; Soci, C.; Abdalla, S.; Abellan, X.; Balsamo, G.; Bechtold, P.; Biavati, G.; Bidlot, J.; Bonavita, M.; Chiara, G.; Dahlgren, P.; Dee, D.; Diamantakis, M.; Dragani, R.; Flemming, J.; Forbes, R.; Fuentes, M.; Geer, A.; Haimberger, L.; Healy, S.; Hogan, R. J.; Hólm, E.; Janisková, M.; Keeley, S.; Laloyaux, P.; Lopez, P.; Lupu, C.; Radnoti, G.; Rosnay, P.; Rozum, I.; Vamborg, F.; Villaume, S.; Thépaut, J. The ERA5 Global Reanalysis. *Quarterly Journal of the Royal Meteorological Society* **2020**, *146* (730), 1999−2049.
(47) de Foy, B.; Cui, Y. Y.; Schauer, J. J.; Janssen, M.; Turne, J. R.; Wiedinmyer, C. Estimating Sources of Elemental and Organic Carbon and Their Temporal Emission Patterns Using a Least Squares Inverse Model and Hourly Measurements from the St. Louis-Midwest Supersite. *Atmos Chem. Phys.* **2015**, *15* (5), 2405−2427.
(48) Wagner, T.; Warnach, S.; Beirle, S.; Bobrowski, N.; Jost, A.; Pukite, J.; Theys, N. Investigation of Three-Dimensional Radiative Transfer Effects for UV-Vis Satellite and Ground-Based Observations of Volcanic Plumes. *Atmos Meas Tech* **2023**, *16* (6), 1609−1662.
(49) Douros, J.; Eskes, H. J.; van Geffen, J. H. G. M. Comparing Sentinel-5P TROPOMI NO2 column observations with the CAMS-regional air quality ensemble. EGUsphere. https://egusphere.copernicus.org/preprints/2022/egusphere-2022-365/ (accessed July 4, 2022).
(50) Lambert, J.-C.; Claas, J.; Stein-Zweers, D.; Ludewig, A.; Loyola, D.; Sneep, M.; Dehn, A. Quarterly Validation Report of the Copernicus Sentinel-5 Precursor Operational Data Products #19; 2023.
(51) Souri, A. H.; Chance, K.; Sun, K.; Liu, X.; Johnson, M. S. Dealing with Spatial Heterogeneity in Pointwise-to-Gridded-Data Comparisons. *Atmos. Meas. Tech* **2022**, *15*, 41−59.


https://doi.org/10.1021/acsestair.4c00097
*ACS EST Air* 2024, 1, 1391−1401